Langmuir-Slow Extraordinary Mode Magnetic Signature Observations with Parker Solar Probe

A. Larosa[1] , T. Dudok de Wit[1] , V. Krasnoselskikh[1,2] , S. D. Bale[2,3] , O. Agapitov[2] , J. Bonnell[2] , C. Froment[1] ,
K. Goetz[4] , P. Harvey[2] , J. Halekas[5] , M. Kretzschmar[1] , R. MacDowall[6] , David M. Malaspina[7,8] , M. Moncuquet[9] ,
J. Niehof[10] , M. Pulupa[2] , and C. Revillet[1]

[1] LPC2E, CNRS, CNES and University of Orléans, 3A avenue de la Recherche Scientifique, Orléans, France; andrea.larosa@cnrs-orleans.fr
[2] Space Sciences Laboratory, University of California, Berkeley, CA 94720-7450, USA
[3] Physics Department, University of California, Berkeley, CA 94720-7300, USA
[4] School of Physics and Astronomy, University of Minnesota, Minneapolis, MN 55455, USA
[5] The University of Iowa, Iowa City, IA 52242, USA
[6] Solar System Exploration Division, NASA/Goddard Space Flight Center, Greenbelt, MD 20771, USA
[7] Astrophysical and Planetary Sciences Department, University of Colorado, Boulder, CO 80305, USA
[8] Laboratory for Atmospheric and Space Physics, University of Colorado, Boulder, CO 80305, USA
[9] LESIA, Observatoire de Paris-Meudon, Meudon, F-92195, France
[10] University of New Hampshire, Institute for the Study of Earth, Oceans, and Space, Space Science Center, Durham, NH 03824, USA

Abstract

Radio emission from interplanetary shocks, planetary foreshocks, and some solar flares occurs in the so-called "plasma emission" framework. The generally accepted scenario begins with electrostatic Langmuir waves that are driven by a suprathermal electron beam on the Landau resonance. These Langmuir waves then mode-convert to freely propagating electromagnetic emissions at the local plasma frequency f_{pe} and/or its harmonic $2f_{pe}$. However, the details of the physics of mode conversion are unclear, and so far the magnetic component of the plasma waves has not been definitively measured. Several spacecraft have measured quasi-monochromatic Langmuir or slow extraordinary modes (sometimes called z-modes) in the solar wind. These coherent waves are expected to have a weak magnetic component, which has never been observed in an unambiguous way. Here we report on the direct measurement of the magnetic signature of these waves using the Search Coil Magnetometer sensor of the Parker Solar Probe/FIELDS instrument. Using simulations of wave propagation in an inhomogeneous plasma, we show that the appearance of the magnetic component of the slow extraordinary mode is highly influenced by the presence of density inhomogeneities that occasionally cause the refractive index to drop to low values where the wave has strong electromagnetic properties.

Unified Astronomy Thesaurus concepts: Solar wind (1534); Plasma physics (2089); Space plasmas (1544)

1. Introduction

Langmuir waves have been routinely observed in the solar wind and in Earth's electron foreshock since the early observations of radio waves in space (Scarf et al. 1971). They are known to be associated with solar radio bursts (Gurnett & Frank 1975) and with electron beams generated at planetary bow shocks (Filbert & Kellogg 1979).

Although these waves, which are part of the Langmuir-slow extraordinary (L-SE) branch, have received considerable attention (Bale et al. 1998; Kasaba et al. 2000; Malaspina & Ergun 2008; Malaspina et al. 2011; Kellogg et al. 2013), there remain many open questions. The waves are generated by a bump-on-tail instability associated with energetic electrons (Lin et al. 1981). However, the mechanisms by which these electrostatic waves are subsequently mode converted into electromagnetic waves still are not fully understood (Hinkel-Lipsker et al. 1991; Kim et al. 2013; Cairns & Layden 2018; Krasnoselskikh et al. 2019, and references therein).

One of the earliest observations of shock-associated Langmuir waves was made by the OGO 5 spacecraft in the 1970s (Scarf et al. 1970). These observations showed evidence of enhancements of the spectral density of the associated magnetic field. However, the anomalously high fundamental frequency of these waves, the lack of waveform measurements, and the low spectral resolution of the instrument (Crook et al. 1969) did not allow evidence of a magnetic signature until now.

More recently, Bale et al. (1998) found by studying the phase relation with the interplanetary magnetic field that these waves are not purely longitudinal as expected for Langmuir waves. They suggested that they are actually slow extraordinary or z-mode waves (Krauss-Varban 1989) driven to low wavenumbers by the WKB propagation effect in solar wind density fluctuations (Bale et al. 2000). Here we prefer the terminology *slow extraordinary mode*.

Malaspina et al. (2011) found a positive correlation between the perpendicular electric field (indicative of a slow extraordinary mode) and the electron beam energy. They supposed that the key ingredient for the production of the L-SE is the reduction of the intensity of the k-vector, which implies a stronger perpendicular electric field. The proposed mechanisms to achieve this decrease involve the presence of positive density gradients and exclude the possibility of electrostatic decay.

Another interesting aspect of the work by Malaspina et al. (2011) is that in the presence of a double peak around the plasma frequency (a common feature) the lower-frequency
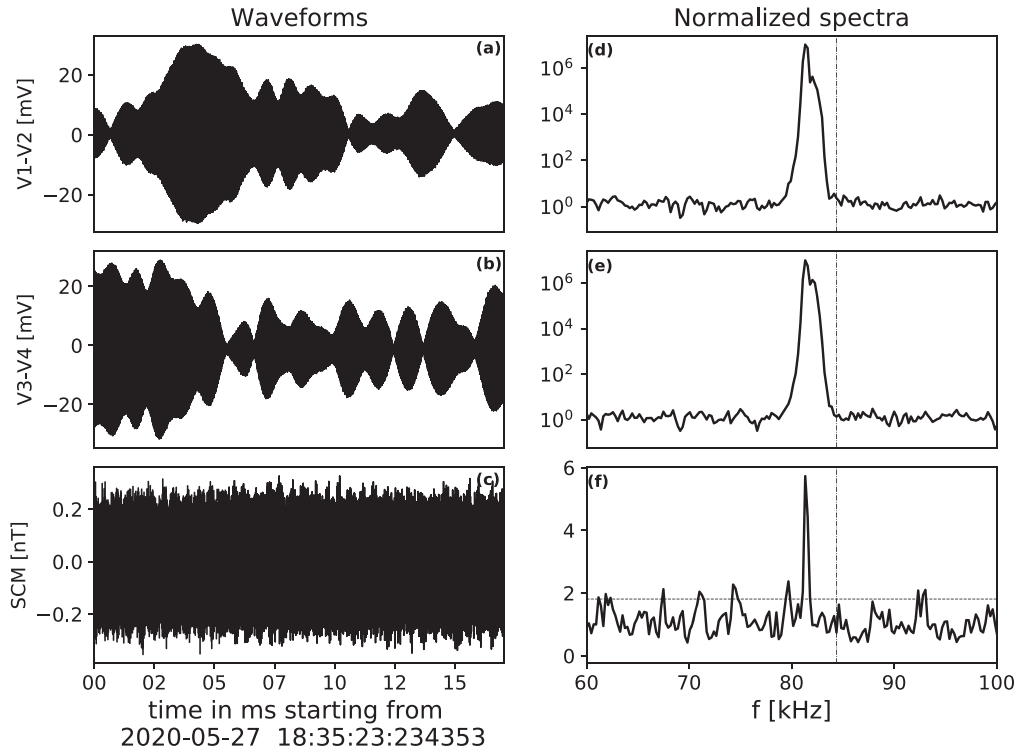
Figure 1. Example of an L-SE wave burst with a magnetic signature. On the left, from top to bottom: raw waveforms from the dipolar electric field $V1 - V2$, $V3 - V4$, and the SCM search coil. On the right, their corresponding normalized power spectral densities. The vertical dashed line indicates the location of the plasma frequency.

peak typically has larger amplitude of the transverse electric field relative to the parallel field.

Evidence for three-wave decay for some bursts was provided by Kellogg et al. (2013), Graham & Cairns (2013), and references therein. Malaspina & Ergun (2008) investigated wave bursts in STEREO observations and concluded that about 75% of the events were linearly polarized. The remaining ones are two-dimensional and three-dimensional structures that can be interpreted as eigenmodes of solar wind density cavities.

In all the studies that we have cited so far the major experimental evidence for the presence of a slow extraordinary mode is the observation of a circularly or elliptically polarized component of the electric field that is perpendicular with respect to the magnetic field. However, we were still lacking direct evidence of a magnetic signature of the L-ES. We report here the first direct and unambiguous experimental observation of this magnetic signature.

2. Data and Methods

Our analysis mainly relies on waveforms sampled by the Time Domain Sampler (TDS) instrument on board Parker Solar Probe (Bale et al. 2016). This instrument provides high-cadence waveforms that are sampled here at 1.92 MHz and last for 17.07 ms. The TDS has five channels. One of them captures the magnetic field from the high-frequency antenna of the Search Coil Magnetometer (SCM; Jannet et al. 2021). The other four channels capture the electric field: two use voltage differences between opposite antennas ($V1 - V2$ and $V3 - V4$), and two use monopole measurements (V3 and V5, which is on the same boom as the SCM). Additionally, a sixth digital channel records electron counts from the SWEAP instrument (Kasper et al. 2016).

Since the launch of Parker Solar Probe in 2018 August, the TDS has been routinely recording bursts, with tens to several hundred events per day depending on the mode of operation. During the first orbit around the Sun, the burst detection algorithm was more sensitive to dust impacts, so that few Langmuir wave events were recorded. This has changed since, from orbit 3 onward, the TDS focuses on waves instead of dust impacts.

The presence of Langmuir wave events in TDS bursts can be readily detected from a peak near the plasma frequency in the power spectral density. For the electric field, the peak amplitudes are generally orders of magnitude above the noise level. For the magnetic field, however, the peak at the same frequency (if any) is much weaker and rarely exceeds the noise level by more than one order of magnitude (Dudok de Wit et al. 2021). In addition, all waveforms, and in particular the magnetic ones, are affected by line interferences that are due to the spacecraft.

To better reveal the presence of narrowband waves in the Fourier spectra, we normalize each spectrum to a typical spectrum for that day, for which we take the 30th percentile of all measurements of the day. That is, for each frequency, we sort all power spectral amplitudes and keep the 30th percentile. The resulting spectrum mainly consists of a noise floor with narrow interference lines. Such lines stick out because they are stable in amplitude and in frequency, in contrast to plasma waves that are eliminated because they drift in frequency. We found the value of 30% to be a good compromise between the median (or 50th percentile), which sometimes has signatures of Langmuir waves, and smaller percentiles, which are increasingly affected by noise. With this normalization our spectra are devoid of interference lines and the magnetic signatures of the L-SE mode are better evidenced. The magnetic signature shown in Figure 1 has been obtained that way.

Langmuir bursts seen by Parker Solar Probe are often preceded by type III solar radio bursts, which are captured by the Radio Frequency Spectrometer (RFS) on board the spacecraft (Pulupa et al. 2017).

In the following, we also consider electron strahl and core properties from observations made by the Solar Wind Electrons Alphas and Protons (SWEAP) instrument suite (Halekas et al. 2020). The count rate of high-energy electrons is provided by the EPI-Lo instrument from the Integrated Science Investigation of the Sun (IS⊙IS) suite (McComas et al. 2016). We integrate the count rate between energies of 29.4 and 234.4 keV and across all arrival directions, to maximize the signal-to-noise ratio. The ion density does not reveal any increase during the interval of interest, so we are confident that we mostly measure energetic electrons. The data release used for IS⊙IS is number 8.

3. Magnetic Signature

We investigated all 30,139 TDS bursts recorded between 2018 October 1 and 2021 May 1 and first isolated all events exhibiting coherent wave packets in the electric field with a frequency located near the plasma frequency. Subsequently, we isolated all events that showed a statistically significant peak (greater than the 95th percentile of the day) in the normalized magnetic field, at the same frequency. We found only 26 of them, all of which occurred on 2020 May 27 (18 events) and 28 (8 events). On those dates, the spacecraft was on its inbound leg of its fifth orbit around the Sun, at a distance of 0.34–0.37 au.

Figure 1 shows a typical example of an L-SE wave burst with a distinctive signature in the normalized magnetic field. In this example, the peak in the power spectral density is 6 times above the noise floor, whereas for the electric field it exceeds the noise floor by more than 6 orders of magnitude. This weak amplitude of the magnetic signature is consistent with the quasi-electrostatic nature of these waves. The three columns on the left show the raw waveforms recorded in the electric field (V1 − V2 and V3 − V4), and in the magnetic field. Note that no coherent wave activity is apparent in the latter because the signal is dominated by interference noise coming from the spacecraft.

The three columns on the right of Figure 1 show the corresponding power spectral densities, estimated by Welch's method. The electric field has a double-peaked spectral signature that has often been observed before in the solar wind (Bale et al. 1996; Krasnoselskikh et al. 2011; Malaspina et al. 2011; Graham & Cairns 2013). These peaks correspond to the incident and reflected wave. Interestingly, in all the events we observed, the spectral peak of magnetic field coincides with the largest of the spectral peaks of the electric field, which is the one that has the lowest frequency and corresponds to the incident wave. The second peak (the reflected wave) might as well have a magnetic signature, which just happens to remain buried in the noise.

Interestingly, these events were preceded by a type III solar radio burst whose energetic electrons provided the necessary conditions for observing L-SE waves. Figure 2 provides a global picture of the plasma conditions on 2020 May 27. Panel (a) displays the magnetic field. Panel (b) shows the spectral amplitude of V1 − V2, as measured by the RFS instrument, with two type III solar radio bursts occurring around 18:10 UT. The outward-propagating electron beam reaches the spacecraft by 18:30 UT. The strong enhancement seen by RFS coincides with the observation of Langmuir wave packets by TDS. The frequency of the latter is reported in panel (c) and tracks the drop in the electron density shown in panel (d). Note that the electron gyrofrequency is much smaller and is around 800 Hz. The last panel reveals a small but statistically significant increase in the number of energetic electrons with energies between 29.4 and 234.4 keV.

The electrons that generate the L-SE mode are expected to have energies between 1 and 3 keV, which is much lower energy than what EPI-Lo can measure. We obtain this estimate in two different ways. First, we assume that the time interval between the beginning of the type III radio burst and the first in situ L-SE burst equals the time required for an electron beam to travel from 1 solar radius ($R_\odot$) to the location of the spacecraft near 80 $R_\odot$ in a radial trajectory. This gives us a velocity and hence an energy of the electron beam in the 1–3 keV range.

We obtain comparable values by considering the density profile as a function of the radial distance from the Sun, using the method by Leblanc et al. (1998). This profile can be converted into a radial profile for the plasma frequency. Using the highest and lowest frequencies of the radio burst, we can invert the formula to obtain the distance from the Sun and, from this, the beam energy.

The electrons observed by EPI-Lo are not the ones that cause the L-SE bursts, since their onset happens about 7 minutes earlier than the first observed electromagnetic burst. However, they are part of the same beam of energetic electrons and therefore provide additional evidence for the existence of such a beam. With this, Figure 2 clearly shows that the L-SE bursts were generated in a highly inhomogeneous plasma. As we shall show next, this is of crucial importance for the presence of magnetic signatures.

4. Theoretical Framework

The key to the understanding of the occurrence of magnetic signatures of the L-SE mode is the relationship between fluctuations of the magnetic field, fluctuations of the electric field, and the value of the refractive index N. The three are related through the Faraday law in Fourier space

$$\delta \boldsymbol{B} = \boldsymbol{N} \times \delta \boldsymbol{E}. \tag{1}$$

In this equation, $\boldsymbol{N}$ is a vector whose magnitude equals the refractive index N and that is directed along the $\boldsymbol{k}$-vector of the wave. This expression suggests that the ratio between electric and magnetic field perturbations is proportional to the refractive index of the wave. However, careful analysis of the polarization properties of the L-SE wave mode shows that (paradoxically) the dependence is roughly inverse. Indeed, from the dispersion relation of a warm magneto-active plasma, combined with Faraday's law, we find (see Appendix A)

$$\delta \boldsymbol{B} \simeq \frac{\delta E}{N} \begin{pmatrix} -i\dfrac{\Omega_c}{\omega_p} \cos\theta \sin\theta \\ 3k^2\lambda_D^2 \cos\theta \sin\theta \\ i\dfrac{\Omega_c}{\omega_p} \sin^2\theta \end{pmatrix}, \tag{2}$$

where θ is the angle between the background magnetic field and $\boldsymbol{k}$, ω_p is the electron plasma frequency, Ω_c is electron cyclotron frequency, and λ_D is the Debye length.
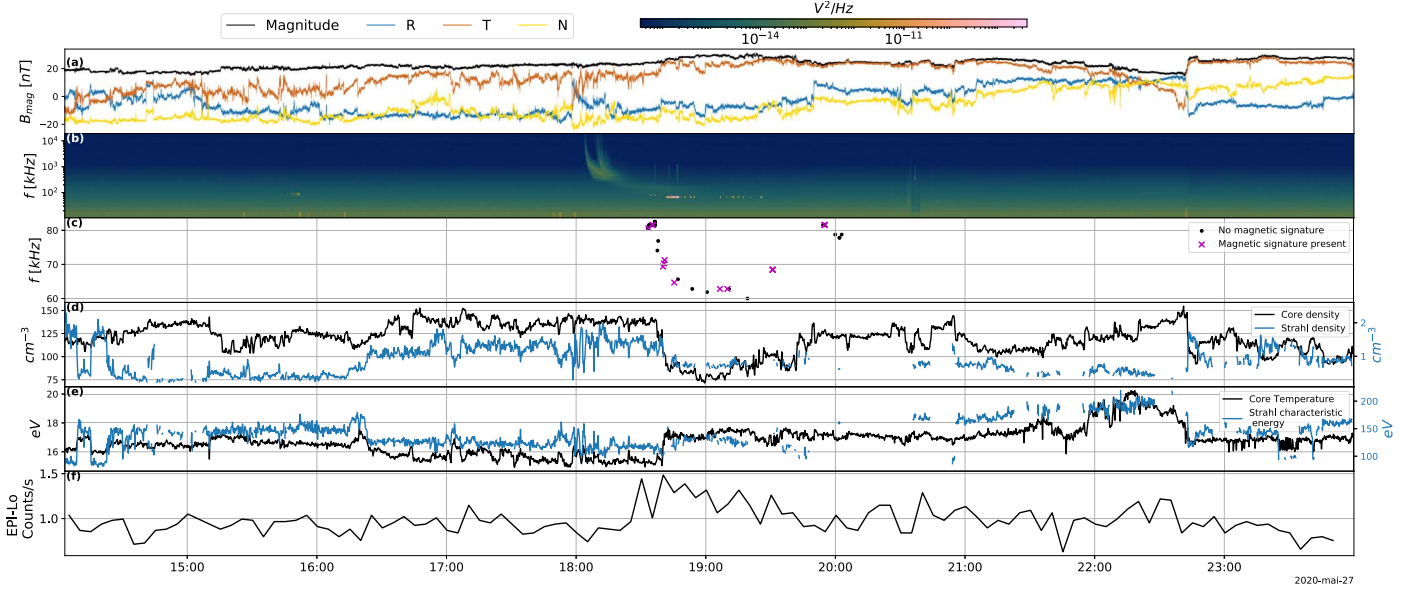
Figure 2. General view of the plasma conditions on 2020 May 27. From top to bottom: (a) the magnetic field from MAG, (b) spectrogram of the V1 − V2 dipole voltage from RFS (with color bar at the top), (c) peak frequency of the L-SE bursts observed by TDS, (d) density of the electron core (black) and strahl (blue) population from SWEAP, (e) electron core temperature (black) and strahl characteristic energy (blue) from SWEAP, and (f) energetic electron counts from EPI-Lo.

In Equation (2) we consider monochromatic fluctuations around the plasma frequency. By taking the modulus on both sides, we obtain the relationship in Fourier space at fixed ω between the fluctuation amplitudes of the magnetic and electric fields and the refractive index. Assuming a small angle of propagation of $\theta = 10°$ (because the modes are mostly electrostatic), $\omega \approx \omega_{pe}$, and estimating $k^2 \lambda_D^2$ as clarified in Section 4.1 and the ratio Ω_c / ω_p from Figure 2, we obtain

$$\delta B^2 \simeq 10^{-5} \frac{\delta E^2}{N^2}. \quad (3)$$

Equation (3) reveals that the conditions for having a strong magnetic component of the wave are the presence of strong electric fluctuations and a small value of the refractive index. The latter typically arises in the presence of inhomogeneities in the plasma. Let us investigate this by studying the propagation of a wave in an inhomogeneous medium.

4.1. Wave Propagation in Inhomogeneous Media: A Hamiltonian Approach

The dispersion relation for quasi-electrostatic slow extraordinary waves may be written as in Equation (4) (Brejzman 1987). Here we neglect the contribution of ions, and without loss of generality the average magnetic field is chosen to be along the z-axis,

$$\omega = \omega_p \left[1 + \frac{3}{2} k_z^2 \lambda_D^2 + \frac{\Omega_c^2}{2\omega_p^2} \sin^2 \theta \left(1 - \frac{\omega^2}{c^2 k^2} \right) \right]. \quad (4)$$

The second term on the right-hand side (rhs) should actually involve $k^2 \lambda_D^2$ (Krasnoselskikh & Sotnikov 1977), but since $k_x^2 \lambda_D^2$ is smaller than all other terms, we omit it in what follows.

The term $k_z^2 \lambda_D^2$ is equal to the ratio v_{th}^2 / v_b^2, assuming a resonant interaction between the electron beam and the wave, i.e., $v_{beam} \approx v_{phase}$. For the events we observe in the solar wind, this ratio is of the order of 10^{-2}. The last term of Equation (4) is of the order of 10^{-4} since the ratio between the plasma and cyclotron frequencies is approximately 10^{-2}. We also have

$\frac{\omega^2}{c^2 k^2} = \frac{1}{N^2} \ll 1$ since the modes we consider are quasi-electrostatic. From these considerations, and as a first-order approximation, we can neglect the last term of Equation (4) and evaluate the variation of the z-component of the wavevector when the wave propagates in an inhomogeneous plasma with a varying density. Assuming that $\delta\omega \approx 0$, we obtain

$$\delta k \simeq - \frac{\delta n}{n} \frac{1}{3 \lambda_D^2 k^2} k_z. \quad (5)$$

Equation (5) shows that when the density fluctuations are of the same order as $k_z^2 \lambda_D^2$ the variations of the k-vector are of the same order of magnitude as the k-vector itself. This implies that k_z goes through zero and therefore the wave gets reflected. The refractive index N reaches its minimum when the wave is reflected, which then also increases the chances of observing magnetic signatures.

These considerations can be deepened by considering that in the case of stationary wave propagation the frequency is constant along the wave path. Therefore, by analogy with energy in mechanical systems, the frequency can be considered as a Hamiltonian function. Let us therefore rewrite the equations of motion using the similarity between the momentum of the particle and the k-vector, with coordinates that have the same meaning as in classical mechanics.

We follow a single wave packet in an inhomogeneous plasma with varying electron density and magnetic field. A more detailed explanation of this kind of approach can be found in Suchy (1981). The Hamilton equations for wave propagation are

$$\frac{d\mathbf{k}}{dt} = - \frac{\partial \omega}{\partial \mathbf{x}} \quad (6a)$$

$$\frac{d\mathbf{x}}{dt} = \mathbf{V}_{gr} = \frac{\partial \omega}{\partial \mathbf{k}}, \quad (6b)$$

where $\mathbf{V}_{gr}$ is the group velocity.

The resulting system of equations in a two-dimensional space, where one direction is parallel to the magnetic field (z)
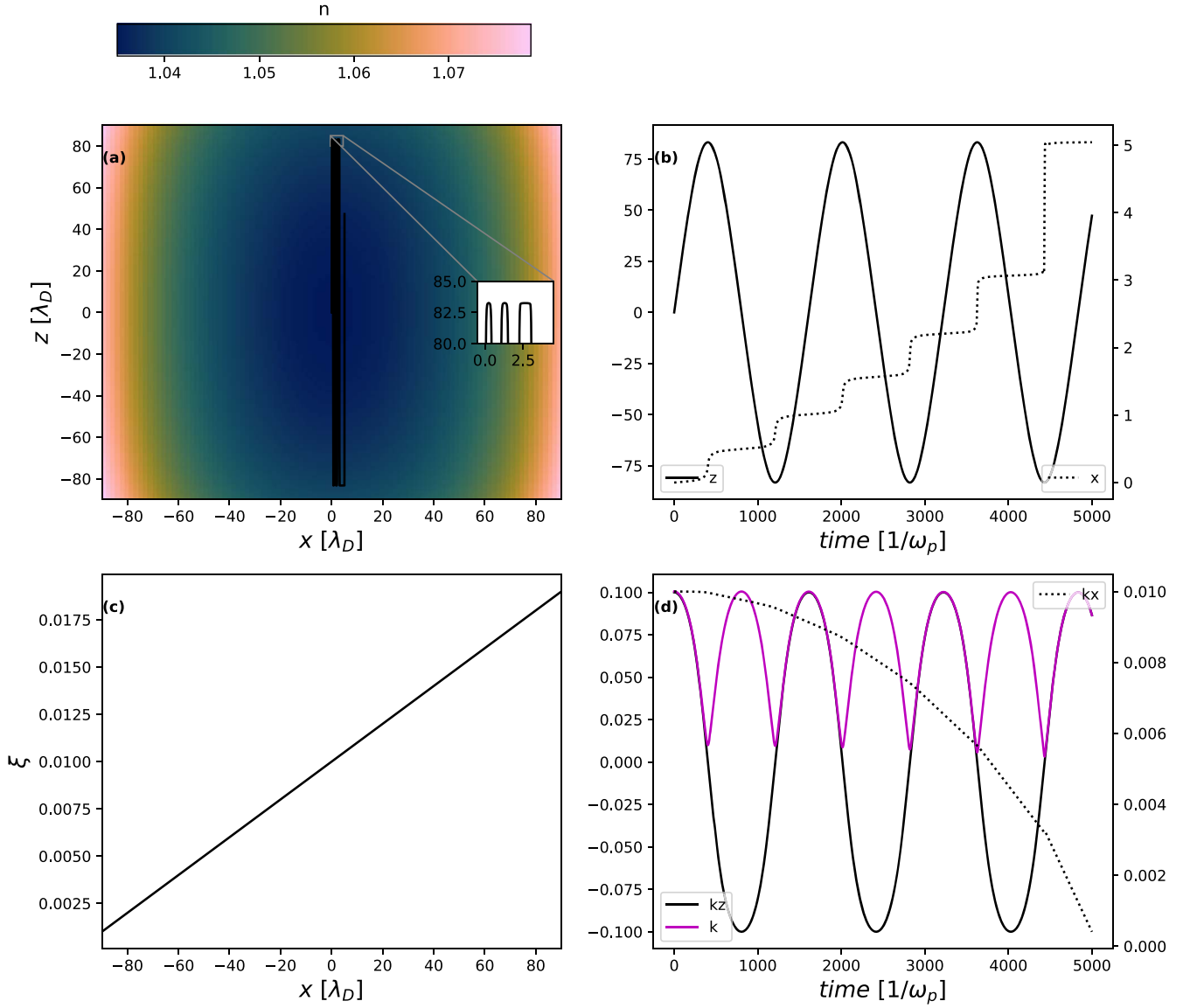
Figure 3. Numerical integration of system (7). Panel (a) shows the density cavity in the x-z plane and the wave trajectory in black. Panel (b) shows the position of the wave with respect to time; the solid line is z, and the dotted line is x. Panel (c) shows the spatial profile of the ξ parameter. Panel (d) shows the components of the k-vector; the solid line is k_z, the dotted line is k_x, and the solid line in magenta is for the magnitude. In panels (b) and (d) the ticks on the left correspond to the quantities whose legends are on the left, and the ticks on the right correspond to legends that appear on the right.

and the other orthogonal to it (x), reads (see Appendix B)

$$\frac{dx}{dt} = \xi^2 \frac{k_x}{k^4}\left[k_z^2 - \frac{v^2}{k^2}(k_z^2 - k_x^2)\right] \qquad (7a)$$

$$\frac{dz}{dt} = 3k_z \qquad (7b)$$

$$\frac{dk_x}{dt} = -\frac{\partial n}{\partial x} - \xi \frac{k_x^2}{k^2}\left(1 - \frac{v^2}{k^2}\right)\frac{\partial \xi}{\partial x} \qquad (7c)$$

$$\frac{dk_z}{dt} = -\frac{1}{2}\frac{\partial n}{\partial z}. \qquad (7d)$$

In Equations (7) all the quantities are dimensionless. Lengths, time, and k-vector are respectively normalized by the Debye length, the electron plasma frequency, and the inverse of the Debye length. The dimensionless density fluctuations n are normalized to the background electron density. The variation of the magnetic field appears in the dimensionless variable $\xi = \frac{\Omega_c}{\omega_p}$. The parameter $v = \frac{v_{th}}{c}$ represents the ratio of the electron thermal speed to the speed of light.

5. Simulation

We simulate the system of Equations (7) on a fixed grid that does not evolve in time, and we study the variation of the refractive index in the presence of prespecified density profile n and changes in the profile of ξ. We solve the equations with a fourth-order Runge–Kutta scheme.

Figure 3 illustrates the evolution of a wave in the presence of a density depletion (along x and z) and a magnetic field that gradually increases along x. We initialize the simulation at $x_0 = 0$ and $z_0 = 0$, $kx_0 = 0.01$ and $kz_0 = 0.1$. The choice of the initial position is arbitrary, while the choice of the initial value of the wavevector is motivated by the fact that the L-SE mode

is mainly parallel to the magnetic field. The assumed beam-plasma interaction gives $k \approx 1/10\lambda_D$ (see Section 4.1), so that a value of 0.1 can be used for the normalized k_z.

The density profile is shown in Figure 3(a). We use a normalized background density of 1 with fluctuations up to 8%. This is consistent with Krupar et al. (2018). The black line represents the trajectory of the wave. The ratio $\xi = \Omega_c/\omega_p$ determines the main motion direction; this ratio is approximately 10^{-2}, and so the motion is mostly along the parallel direction z. The inset highlights the reflection of the wave. The density cavity is given by the model $n(x, z) = 1 + \alpha \exp((x/l)^2) + \beta \exp((z/l)^2)$. We set $l = 100$ to have a length scale for the variation of the density profile that is much larger than the wavelength, in agreement with the WKB approximation. The parameters α and β are used to tune the level of density fluctuations in the two directions. In Figure 3 $\alpha = \frac{\beta}{6}$ to allow the wave to propagate more along the x-direction before being reflected toward $-x$. Our objective is to obtain more minima of the k-vector in panel (d), to ease visualization.

Panel (c) shows the dimensionless variable $\xi = \frac{\Omega_c}{\omega_p}$, which expresses the profile of the magnetic field. The increase is chosen consistently with the one observed in the data of Figure 2, with a profile that is given by $\xi = 10^{-2} \cdot (1 + x/l)$. The factor 10^{-2} represents the ratio between gyrofrequency and plasma frequency.

Panel (b) shows the position versus time of the wave on the grid. The periodic variation of the z-component and the drift in the x-direction are evident. This drift is enhanced at the reflection points, and it increases, from one reflection to the next, when the wave moves toward positive x owing to increasing ξ values.

Panel (d) shows that k (and therefore the refractive index) is lowest at the reflection points. The drop is of the order of 90%, which corresponds to a drop of 99% in N^2. This in turn implies that the magnetic component is largest at the reflection points, as suggested by Equation (2). Furthermore, the ratio k_x/k_z is larger at the reflection points, which means that relatively more power goes in the perpendicular direction at the reflection point, in agreement with the observations made by Malaspina et al. (2011).

6. Discussion and Conclusion

We report the first unambiguous observation of magnetic signatures associated with the extraordinary slow wave mode (or z-mode) in the solar wind. In 2.5 yr of observations by Parker Solar Probe, we have found only 2 days with significant evidence of such magnetic signatures.

The observed events occurred during conditions of strong density fluctuations and took place when the spacecraft was located close to an electron beam associated with a type III solar radio burst.

To interpret these results, we investigated the analytical relation between the level of magnetic and electric fluctuations and the refractive index N of the waves. The inverse proportionality between N and the ratio $\delta B/\delta E$ indicates that in inhomogeneous media variations in N substantially affect wave propagation.

To put this on firmer ground, we studied the Hamilton equation for the propagation of a single wave and, by simulating this equation, found that in the presence of density

depletions a drop in the refractive index occurs at the reflection point of the wave.

These results raise the question as to why such magnetic signatures are so rare. First, let us stress that Parker Solar Probe and Solar Orbiter are the first modern missions whose magnetic sensor covers the frequency range of Langmuir waves; no systematic study had been carried out beforehand in the solar wind. Furthermore, the vast majority of Langmuir waves that have been observed by Parker Solar Probe do not coincide with type III radio bursts. Therefore, the ratio of the beam velocity with respect to the thermal velocity is generally very small, which decreases the chances of observing the magnetic signatures of the L/SE modes.

Another important element here is the sensitivity of the instrument chain, which has two contributions. One comes from the sensitivity or noise floor of the SCM, which is 0.01 pT Hz$^{-1/2}$ in the frequency range of interest. The other is the resolution of the TDS, which is 0.05 mV and is equivalent to 0.1 pT. From this we conclude that the observability of magnetic signatures is primarily constrained by the resolution of the TDS. As shown by Dudok de Wit et al. (2021), the magnitude of the magnetic signature is bounded by that of the electric fluctuations $\delta B \leqslant \alpha \delta E$, where α is a constant. The events that have a distinct magnetic signature correspond to the largest values of δE observed by Parker Solar Probe. This suggests that many more events may potentially have a magnetic signature but just happen to be too weak to exceed the 100 fT noise floor.

Similarly, the coherent wave packets show two peaks in the power spectral density of δE with a magnetic signature that always coincides with the lowest-frequency peak, i.e., the incident wave. Again, we cannot conclude whether the reflected wave also has a magnetic signature, as the amplitude of the latter remains well below the noise floor.

Appendix A
Relation between B, E, and N

The linearized Vlasov–Maxwell system in Fourier space for a cold plasma can be written as (see Akhiezer et al. 1975, Equation (4.3.1.10))

$$\begin{pmatrix} \varepsilon_1 - \dfrac{k_z^2 c^2}{\omega^2} & -i\varepsilon_2 & \dfrac{k_x k_z c^2}{\omega^2} \\ i\varepsilon_2 & \varepsilon_1 - \dfrac{k^2 c^2}{\omega^2} & 0 \\ \dfrac{k_x k_z c^2}{\omega^2} & 0 & \varepsilon_3 - \dfrac{k_x^2 c^2}{\omega^2} \end{pmatrix} \begin{pmatrix} \delta E_x \\ \delta E_y \\ \delta E_z \end{pmatrix} = 0. \quad (A1)$$

Here the magnetic field is along the z-direction and the k-vector in the x-z plane; k_x, k_z, and k respectively denote the x component, the z-component, and the magnitude of the k-vector; c is the speed of light and ω the wave pulsation; and ε_1, ε_2, and ε_3 are the elements of the dielectric permittivity tensor for a cold plasma (see Akhiezer et al. 1975 Equation (5.1.1.5)).

Note that in ε_3 we consider the contribution of the electron temperature, through the term $3k^2\lambda_D^2$, which is the largest input in the limit of $\omega_p \gg \Omega_c$.

The following equations refer to a single species; indeed, we neglect the contribution of the ions since we are interested in high-frequency waves:

$$\varepsilon_1 = 1 - \frac{\omega_p^2}{\omega^2 - \Omega_c^2} \quad \varepsilon_2 = -\frac{\omega_p^2\Omega_c}{\omega(\omega^2 - \Omega_c^2)}$$

$$\varepsilon_3 = 1 - \frac{\omega_p^2(1 + 3k^2\lambda_D^2)}{\omega^2}. \tag{A2}$$

From the system of Equation (A1) we obtain two components of the electric field as functions of the third one. The matrix must not have maximum rank in order to avoid trivial solutions. The choice of E_z as the free component leads to Equation (A3), in which $N = \frac{kc}{\omega}$ is the refractive index.

$$\delta \boldsymbol{E} = \begin{pmatrix} -\dfrac{(\varepsilon_3 - N^2\sin^2\theta)}{N^2\sin\theta\cos\theta} \\ i\dfrac{\varepsilon_2}{(\varepsilon_1 - N^2)}\dfrac{(\varepsilon_3 - N^2\sin^2\theta)}{N^2\sin\theta\cos\theta} \\ 1 \end{pmatrix} \delta E_z. \tag{A3}$$

Let us rewrite Equation (A3) as

$$N^2\sin\theta\cos\theta\delta\boldsymbol{E} = \begin{pmatrix} -(\varepsilon_3 - N^2\sin^2\theta) \\ i\dfrac{\varepsilon_2(\varepsilon_3 - N^2\sin^2\theta)}{(\varepsilon_1 - N^2)} \\ N^2\sin\theta\cos\theta \end{pmatrix} \delta E_z,$$

which, considering that $N \gg 1$, becomes

$$N^2\sin\theta\cos\theta\ \delta\boldsymbol{E} = \begin{pmatrix} N^2\sin^2\theta - \varepsilon_3 \\ \dfrac{i\varepsilon_2}{N^2}\left(1 + \dfrac{\varepsilon_1}{N^2}\right)(N^2\sin^2\theta - \varepsilon_3) \\ N^2\sin\theta\cos\theta \end{pmatrix} \delta E_z.$$

We use this last expression in the Faraday equation in Fourier space in order to have a relation between the electric and magnetic fields and the refractive index. We have $\delta\boldsymbol{B} = N \times \delta\boldsymbol{E}$. When multiplying both sides by $N^2\sin\theta\cos\theta$, we obtain

$$N^2\sin\theta\cos\theta\delta\boldsymbol{B}$$
$$= \begin{pmatrix} -i\dfrac{\varepsilon_2}{N^2}(1 + \dfrac{\varepsilon_1}{N^2})(N^2\sin^2\theta - \varepsilon_3)N\cos\theta \\ -N\cos\theta\varepsilon_3 \\ iN\sin\theta\dfrac{\varepsilon_2}{N^2}(1 + \dfrac{\varepsilon_1}{N^2})(N^2\sin^2\theta - \varepsilon_3) \end{pmatrix} \delta E_z.$$

Let us simplify this equation by making some approximations, considering that $N \gg \varepsilon_1$:

$$\delta\boldsymbol{B} \simeq \begin{pmatrix} -i\dfrac{\varepsilon_2}{N^3\sin\theta}(N^2\sin^2\theta - \varepsilon_3) \\ -\dfrac{\varepsilon_3}{N\sin\theta} \\ i\dfrac{1}{N^3\cos\theta}\varepsilon_2(N^2\sin^2\theta - \varepsilon_3) \end{pmatrix} \delta E_z. \tag{A4}$$

At this point it is useful to consider the explicit form of ε_3 using the dispersion relation in Equation (4):

$$\varepsilon_3 = 1 - \frac{\omega_p^2(1 + 3k^2\lambda_D^2)}{\omega^2}$$

$$= \frac{\omega_p^2(1 + 3k_z^2\lambda_D^2) + \Omega_c^2\sin^2\theta\left(1 - \dfrac{\omega_p^2}{k^2c^2}\right) - \omega_p^2(1 + 3k^2\lambda_D^2)}{\omega^2}$$

$$= \frac{-3k^2\lambda_D^2\omega_p^2\sin^2\theta + \Omega_c^2\sin^2\theta\left(1 - \dfrac{\omega_p^2}{k^2c^2}\right)}{\omega^2}$$

$$= \left[-3k^2\lambda_D^2 + \frac{\Omega_c^2}{\omega_p^2}\left(1 - \frac{\omega_p^2}{k^2c^2}\right)\right]\sin^2\theta. \tag{A5}$$

Equation (A5) reveals (taking into account the considerations of Section 4.1) that ε_3 is much smaller than 1. This allows us to approximate the term $N^2\sin^2\theta - \varepsilon_3$ as $N^2\sin^2\theta$ in Equation (A4). Considering that $\delta E_z = \delta E\cos\theta$, $\varepsilon_2 \simeq \frac{\Omega_c}{\omega_p}$ and using ε_3 from Equation (A5), (A4) now reads:

$$\delta\boldsymbol{B} \simeq \begin{pmatrix} -i\dfrac{\Omega_c}{\omega_p}\dfrac{\cos\theta\sin\theta}{N} \\ -\dfrac{\cos\theta\sin\theta}{N}\left[-3k^2\lambda_D^2 + \dfrac{\Omega_c^2}{\omega_p^2}\left(1 - \dfrac{\omega_p^2}{k^2c^2}\right)\right] \\ i\dfrac{\Omega_c}{\omega_p}\dfrac{\sin^2\theta}{N} \end{pmatrix} \delta E. \tag{A6}$$

Following the considerations made in Section 4.1, we know that $k^2\lambda_D^2 \gg \frac{\Omega_c^2}{\omega_p^2}$. For that reason, we can further approximate Equation (A6) and obtain our final result for the magnetic field component of the slow extraordinary wave:

$$\delta\boldsymbol{B} \simeq \begin{pmatrix} -i\dfrac{\Omega_c}{\omega_p}\dfrac{\cos\theta\sin\theta}{N} \\ 3k^2\lambda_D^2\dfrac{\cos\theta\sin\theta}{N} \\ i\dfrac{\Omega_c}{\omega_p}\dfrac{\sin^2\theta}{N} \end{pmatrix} \delta E.$$

As expected, all components vanish if $\sin\theta = 0$.

Appendix B
Hamiltonian System

In this appendix we detail the calculations to obtain Equation (7). We can rewrite Equation (4), reminding the

reader that $k_z = k \cos \theta$, $k_x = k \sin \theta$ and that $\omega \simeq \omega_p$:

$$\omega = \omega_p \left[1 + \frac{3}{2} k_z^2 \lambda_D^2 + \frac{\Omega_c^2}{2\omega_p^2} \frac{k_x^2}{k^2} \left(1 - \frac{\omega_p^2}{c^2 k^2} \right) \right]. \quad \text{(B1)}$$

The Hamiltonian system (6) expressed in components reads

$$\frac{dk_x}{dt} = -\frac{\partial \omega}{\partial x} \quad \text{(B2a)}$$

$$\frac{dk_z}{dt} = -\frac{\partial \omega}{\partial z} \quad \text{(B2b)}$$

$$\frac{dx}{dt} = V_{gr_x} = \frac{\partial \omega}{\partial k_x} \quad \text{(B2c)}$$

$$\frac{dz}{dt} = V_{gr_z} = \frac{\partial \omega}{\partial k_z}. \quad \text{(B2d)}$$

We calculate the derivatives of system (B2) by assuming a constant electron temperature and by keeping only the most important terms with respect to the derivative of the density and of the electron cyclotron frequency. For example, in the derivative of Equation B2(b) we neglect the term proportional to the density derivative that we would obtain by derivation of ω_p in the third term of Equation (B1). We neglect it because the major contribution due to density variations is in the first term on the rhs. The same applies to the derivative of the term $k_z^2 \lambda_D^2$.

Following these considerations, Equation B2(b) becomes

$$\frac{dk_z}{dt} = -\frac{\omega_p}{2n} \frac{\partial n}{\partial z} - \frac{\Omega_c^2}{\omega_p^2} \frac{k_x^2}{k^2} \left(1 - \frac{\omega_p^2}{k^2 c^2} \right) \frac{\partial \Omega_c}{\partial z}. \quad \text{(B3)}$$

Since the magnetic field is unidirectional and solenoidal, $\frac{\partial \Omega_c}{\partial z}$ must vanish, and so Equation (B3) reads

$$\frac{dk_z}{dt} = -\frac{\omega_p}{2n} \frac{\partial n}{\partial z}. \quad \text{(B4)}$$

In Equation B2(d), the rhs is equal to $3\omega_p \lambda_D^2 k_z$. Now we consider Equation B2(c), in which the explicit form of the rhs is

$$\begin{aligned} \frac{\partial \omega}{\partial k_x} &= \frac{\Omega_p^2}{2\omega_p} \frac{\partial}{\partial k_x} \left(\frac{k_x^2}{k^2} - \frac{\omega_p^2}{c^2} \frac{k_x^2}{k^4} \right) \\ &= \frac{\Omega_p^2}{\omega_p} \frac{k_x}{k^4} \left(k_z^2 - \frac{\omega_p^2}{c^2} \frac{k^2 - 2k_x^2}{k^2} \right) \\ &= \frac{\Omega_p^2}{\omega_p} \frac{k_x}{k^4} \left(k_z^2 - \frac{\omega_p^2}{c^2} \frac{k_z^2 - k_x^2}{k^2} \right). \end{aligned} \quad \text{(B5)}$$

The derivative on the rhs of Equation B2(a) is expressed as

$$\frac{\partial \omega}{\partial x} = \frac{\omega_p}{2n} \frac{\partial n}{\partial x} + \frac{\Omega_c}{\omega_p} \frac{k_x^2}{k^2} \left(1 - \frac{\omega_p^2}{k^2 c^2} \right) \frac{\partial \Omega_c}{\partial x}. \quad \text{(B6)}$$

The system (B7) then reads

$$\frac{dk_x}{dt} = \frac{\omega_p}{2n} \frac{\partial n}{\partial x} + \frac{\Omega_c}{\omega_p} \frac{k_x^2}{k^2} \left(1 - \frac{\omega_p^2}{k^2 c^2} \right) \frac{\partial \Omega_c}{\partial x} \quad \text{(B7a)}$$

$$\frac{dk_z}{dt} = -\frac{\omega_p}{2n} \frac{\partial n}{\partial z} \quad \text{(B7b)}$$

$$\frac{dx}{dt} = \frac{\Omega_p^2}{\omega_p} \frac{k_x}{k^4} \left(k_z^2 - \frac{\omega_p^2}{c^2} \frac{k_z^2 - k_x^2}{k^2} \right) \quad \text{(B7c)}$$

$$\frac{dz}{dt} = \omega_p \lambda_D^2 k_z. \quad \text{(B7d)}$$

To perform a numerical simulation, we normalize system (B7) using the dimensionless variables $\hat{k} = k \lambda_D$, $\hat{t} = t \omega_p$, $\hat{x} = \frac{x}{\lambda_D}$, $\hat{z} = \frac{z}{\lambda_D}$. We introduce the variable $\xi = \frac{\Omega_c}{\omega_p}$ and the constant $v = \frac{v_{th}}{c}$. Using these definitions in Equation (B7), we obtain the normalized system of Equation (7).

ORCID iDs

A. Larosa ⓘ https://orcid.org/0000-0002-7653-9147
T. Dudok de Wit ⓘ https://orcid.org/0000-0002-4401-0943
V. Krasnoselskikh ⓘ https://orcid.org/0000-0002-6809-6219
S. D. Bale ⓘ https://orcid.org/0000-0002-1989-3596
O. Agapitov ⓘ https://orcid.org/0000-0001-6427-1596
J. Bonnell ⓘ https://orcid.org/0000-0002-0675-7907
C. Froment ⓘ https://orcid.org/0000-0001-5315-2890
K. Goetz ⓘ https://orcid.org/0000-0003-0420-3633
P. Harvey ⓘ https://orcid.org/0000-0002-6938-0166
J. Halekas ⓘ https://orcid.org/0000-0001-5258-6128
M. Kretzschmar ⓘ https://orcid.org/0000-0001-5796-6138
R. MacDowall ⓘ https://orcid.org/0000-0003-3112-4201
David M. Malaspina ⓘ https://orcid.org/0000-0003-1191-1558
M. Moncuquet ⓘ https://orcid.org/0000-0002-9621-0365
J. Niehof ⓘ https://orcid.org/0000-0001-6286-5809
M. Pulupa ⓘ https://orcid.org/0000-0002-1573-7457
C. Revillet ⓘ https://orcid.org/0000-0003-4582-7055

References

Akhiezer, A. I., Akhiezer, I. A., Polovin, R. V., Sitenko, A. G., & Stepanov, K. N. 1975, Plasma Electrodynamics, Vol. 1 (Oxford: Pergamon)
Bale, S. D., Burgess, D., Kellogg, P. J., et al. 1996, GeoRL, 23, 109
Bale, S. D., Goetz, K., Harvey, P. R., et al. 2016, SSRv, 204, 49
Bale, S. D., Kellogg, P. J., Goetz, K., & Monson, S. J. 1998, GeoRL, 25, 9
Bale, S. D., Larson, D. E., Lin, R. P., et al. 2000, JGRA, 105, 27353
Brejzman, B. N. 1987, in Problems on Plasma Theory, Vol. 15 ed. B. B. Kadomtsev (Moscow: Energoatomizdat), 55
Cairns, I. H., & Layden, A. 2018, PhPl, 25, 082309
Crook, G., Scarf, F., Fredricks, R., Green, I., & Lukas, P. 1969, ITGE, 7, 120
Dudok de Wit, T., Agapitov, O., Froment, C., et al. 2021, JGR, submitted
Filbert, P. C., & Kellogg, P. J. 1979, JGRA, 84, 1369
Graham, D. B., & Cairns, I. H. 2013, JGRA, 118, 3968
Gurnett, D. A., & Frank, L. A. 1975, SoPh, 45, 477
Halekas, J. S., Whittlesey, P., Larson, D. E., et al. 2020, ApJS, 246, 22
Hinkel-Lipsker, D. E., Fried, B. D., & Morales, G. J. 1991, PhRvL, 66, 1862
Jannet, G., Dudok de Wit, T., Krasnoselskikh, V., et al. 2021, JGRA, 126, e28543
Kasaba, Y., Matsumoto, H., Omura, Y., et al. 2000, JGRA, 105, 79
Kasper, J. C., Abiad, R., Austin, G., et al. 2016, SSRv, 204, 131
Kellogg, P. J., Goetz, K., Monson, S. J., & Opitz, A. 2013, JGRA, 118, 4766
Kim, E.-H., Cairns, I. H., & Johnson, J. R. 2013, PhPl, 20, 122103
Krasnoselskikh, V., Voshchepynets, A., & Maksimovic, M. 2019, ApJ, 879, 51
Krasnoselskikh, V. V., Dudok de Wit, T., & Bale, S. D. 2011, AnGeo, 29, 613
Krasnoselskikh, V. V., & Sotnikov, V. I. 1977, SvJPP, 3, 491
Krauss-Varban, D. 1989, JGRA, 94, 3527
Krupar, V., Maksimovic, M., Kontar, E. P., et al. 2018, ApJ, 857, 82
Leblanc, Y., Dulk, G. A., & Bougeret, J.-L. 1998, SoPh, 183, 165
Lin, R. P., Potter, D. W., Gurnett, D. A., & Scarf, F. L. 1981, ApJ, 251, 364
Malaspina, D. M., Cairns, I. H., & Ergun, R. E. 2011, GeoRL, 38, L13101
Malaspina, D. M., & Ergun, R. E. 2008, JGRA, 113, A12108
McComas, D. J., Alexander, N., Angold, N., et al. 2016, SSRv, 204, 187
Pulupa, M., Bale, S. D., Bonnell, J. W., et al. 2017, JGRA, 122, 2836
Scarf, F. L., Fredricks, R. W., Frank, L. A., & Neugebauer, M. 1971, JGR, 76, 5162
Scarf, F. L., Fredricks, R. W., Green, I. M., & Neugebauer, M. 1970, JGR, 75, 3735
Suchy, K. 1981, RaSc, 16, 1179